TWO-DIMENSIONAL AERODYNAMIC ANAYSIS OF FLIGHT IN THE SMALLEST INSECTS

05

Hrithik Aghav, Laura A. Miller

Abstract:

Two-dimensional immersed boundary simulations were performed to determine how stroke plane angle and wing flexibility affect aerodynamic efficiency and energy efficiency for the smallest flying insects (here boundary refers to the boundary of the elastic structure immersed in the fluid). Extensive experimental data pertaining to small insect flight is unavailable due to the difficulties associated with directly observing the flight of the smallest insects and therefore, their flight mechanisms are still largely unknown. The immersed boundary method was used to solve the fully coupled fluid-structure interaction problem of a flexible wing immersed in a two-dimensional viscous fluid. We considered five different strokes: a horizontal stroke, three different hybrid strokes, and a vertical stroke. We also considered five different wing flexibilities ranging from rigid to highly flexible. Aerodynamic efficiency was defined as the ratio of the average vertical force coefficient to the average total force coefficient and energy efficiency was defined as the ratio of the average vertical force generated by a wing to the average power delivered by the wing to the surrounding fluid. The results indicate that at Reynolds numbers (Re) relevant to small insect flight (4 – 60), both aerodynamic efficiency and energy efficiency decrease with increasing stroke plane angle regardless of wing flexibility.

© 2022 Hrithik Aghav, Laura A. Miller

This article is licensed under a Creative Commons Attribution 4.0 International license.

At Re pertinent to small insect flight, a rigid wing is aerodynamically as well as energetically more efficient than flexible wings at all stroke plane angles. This suggests that a rigid wing with a horizontal stroke could be aerodynamically as well as energetically the most efficient wing flexibility and stroke plane angle combination in the flight of the smallest insects.

Keywords: **Immersed Boundary Method, Computational Fluid Dynamics, Small Insect Flight**

Introduction

Insect flight has been a topic of interest for biologists and physicists for more than a century (Wang, 2005). There are several reasons why research pertaining to insect flight is considered important. For instance, insect flight research can aid in the understanding of the mechanisms that govern insect dispersal by flight. Dispersal is an important topic in entomology and its understanding can facilitate progress in the areas of population genetics, biogeography, pest management, and biodiversity among many others (Naranjo, 2019; Bodino et al., 2021; Cameron et al., 2013). The smallest flying insects are of significant agricultural importance and understanding their flight mechanisms may aid in the biological control of agricultural pests (Jones et al., 2015). For instance, the smallest flying insects include parasitoid wasps which are well-known biological control agents for arthropod pests in agricultural and forest ecosystems (Wang et al., 2019). A comprehensive understanding of the aerodynamics of parasitoid wasps could lead to better strategies for the control of arthropod pests. Thrips are another class of smallest insects that are known to infect cotton seedlings in the United States and are a huge challenge to deal with for growers (Cook et al., 2011). Insights into their flight mechanisms could assist in the development of techniques for limiting the damage they cause to agricultural crops. Engineers are also interested in insect flight research because of its utility in the design of micro-aerial vehicles (MAVs). In recent years, bio-inspired flapping-wing MAVs have been developed, thus, demonstrating the feasibility of flapping wing drones whose sizes are like those of insects (Liu et al., 2016). As can be deduced, research related to insect flight is of both agricultural and engineering importance.

List of Symbols

Re	Reynolds Number	k_S	Spring Stiffness
ρ	Fluid Density	R_L	Spring Resting Length
μ	Dynamic Viscosity	E_{spring}	Spring Elastic Potential Energy
c	Wing Chord Length	F_{spring}	Spring Deformation Energy
U	Wing Tip Velocity	k_{NIB}	Non-invariant beam bending stiffness
A_o	Stroke Amplitude	$\mathbf{F}_{\text{beam}}$	Non-invariant beam deformation force
f	Stroke Frequency	$\delta(\mathbf{x})$	Two-Dimensional Delta Function
β	Stroke Plane Angle	$\mathbf{X}(n,t)$	Cartesian Coordinates of the Material Point
α	Angle of Attack	U_{max}	Maximum Velocity of the Wing Chord Center
α_o	Mean Angle of Attack	U_{rms}	RMS Velocity of the Wing Chord Center
B	Rotation Amplitude	F_V	Vertical Force
$\mathbf{x}$	Eulerian Position (x,y)	F_H	Horizontal Force
$\mathbf{u}(\mathbf{x},t)$	Fluid Velocity	C_V	Vertical Force Coefficient
$p(\mathbf{x},t)$	Fluid Pressure	C_H	Horizontal Force Coefficient
$\mathbf{f}(\mathbf{x},t)$	Force per unit area	C_T	Total Force Coefficient
$\mathbf{F}(n,t)$	Force per unit length	$\overline{C_V}$	Average Vertical Force Coefficient
n	Lagrangian Position	$\overline{C_H}$	Average Horizontal Force Coefficient
t	Time	$\overline{C_T}$	Average Total Force Coefficient
$\mathbf{X}_M$	Lagrangian Point Coordinate	P	Power delivered by the wing to the fluid
$\mathbf{X}_M{}^T$	Target Point Coordinate		
$\mathbf{X}_{SL}$	Slave Node Coordinate		
k_T	Stiff Spring Stiffness		
$\mathbf{F}_T$	Stiff Spring Deformation Force		
E_T	Stiff Spring Deformation Energy		

It has been known for a long time that the aerodynamics and flight dynamics of insect flight are significantly different from those of fixed-wing aircraft (Wang, 2004; Ellington, 1999). Fixed-wing airplanes generally execute steady, level flight at small angles of attack and therefore, primarily utilize aerodynamic lift to generate the weigh-supporting vertical force.

It has been observed, however, that insects pitch their wings at large angles of attack to remain airborne (Wang, 2004). This, coupled with the fact that insect flight is unsteady, requires us to move away from classical aircraft aerodynamics and develop novel techniques for understanding insect flight (Ellington, 1999). A variety of experimental studies (Jensen, 1956; Cloupeau et al., 1979; Wilkin and Williams, 1993; Hollick, 1940; Nachtigall, 1973) and theoretical analyses (Demoll, 1919; Weis-Fogh and Jensen, 1956; Von Holst and Kuchemann, 1942) have been carried out in the past century to try and unravel the complexities of insect flight. Most of the early theoretical work was based on quasi-steady analysis where the main assumption is that the instantaneous forces on a wing are determined by its current state of motion and are independent of its flight history.

Multiple experimental studies (Cloupeau et al., 1979; Wilkin and Williams, 1993; Dudley and Ellington, 1990; Vogel, 1967) have proved that this approach fails to explain the flight strategies employed by insects. More recent theoretical work has focused on important unsteady phenomena in flapping flight aerodynamics such as leading-edge vortex (LEV) to shed light on the aerodynamics of insects and birds (Nabawy and Crowther, 2017; Eldredge and Jones, 2019). Such theoretical work produces low-order analytical models that provide insights into the flow physics of flapping flight that are not available from higher-order computational methods (Nabawy and Crowther, 2017). Here order refers to the complexity of the model. A low order model is a simplification of a high-fidelity complex model. Along with more accurate theoretical models, many other methodologies have been developed and utilized to probe insect flight.

Computational fluid dynamics tools have been developed and employed to reveal the three-dimensional aerodynamics of insect flight. Their emergence was accompanied by the development of novel experimental techniques for probing insect flight (Ellington et al., 1996; Dickinson et al., 1999). All these developments have contributed immensely to our understanding of flight techniques employed by insects ranging in size from Drosophila to dragonflies. However, we haven't yet developed a comprehensive understanding of flight in the smallest insects. We are only now beginning to understand the flight mechanisms employed by the smallest insects (Williams and Murphy, 2020; Sarig and Ribak, 2021; Burrows and Dorosenko, 2019). It has been observed that the flight mechanisms employed by the smallest insects are significantly different from those employed by large insects (Miller and Peskin, 2004, 2005, 2009; Wang, 2000) and therefore, the smallest insects demand special attention. The flight of the smallest insects is different from that of large insects in that they fly at low Re (4 - 60) and flap their wings at very high frequencies - frequencies as high as 400 Hz (Weis Fogh, 1973). At such low Re, viscous effects are quite significant. Here "significant" means that the viscous forces cannot be neglected relative to the inertial forces. The Re is a measure of the ratio of inertial forces to viscous forces in fluid flows. In high Re flows, the inertial forces are significantly larger than the viscous forces and therefore, inviscid flow models and the Euler equations can be utilized to model the flow and obtain quantities like lift and moment coefficients. A low Re indicates that the inertial and viscous forces are of comparable magnitudes and therefore, it becomes essential to avoid using inviscid flow assumptions while modeling low Re flows. A notable example that illustrates this is Lighthill's 1973 paper where inviscid flow assumptions for the clap and fling mechanism at low Re resulted in lower forces than those obtained without making any simplifying assumptions about the viscous effects (Lighthill, 1973).

Experimental data pertaining to flight in the smallest insects is highly limited due to the small size of these insects and the difficulties associated with observing their flight in nature (Sane, 2003). The available experimental data for certain small insects indicates that tiny insects utilize the clap and fling mechanism during flight (Weis-Fogh, 1973; Ellington, 1984; Miller and Peskin, 2009). However, it is not clear if this is the only mechanism employed by the smallest insects.

The lack of extensive experimental data related to small insect flight has sparked debates and led to speculation about the flight strategies employed by these insects (Jones et al., 2015). Lift-based strokes in the horizontal plane and drag-based strokes in the vertical plane have been suggested as possible flight mechanisms. Here horizontal plane is perpendicular to the direction of gravity and vertical plane is parallel to the direction of gravity. Weis-Fogh's 1973 paper popularized lift-based strokes through its description of the clap and fling mechanism (Weis-Fogh, 1973). In this mechanism, the insect "claps" its wings at the end of the upstroke and "flings" them apart at the beginning of the downstroke. At the scale of tiny insects, this motion generates more vertical force coefficient than the wing kinematics utilized by large insects and birds. However, the main issue with this strategy is that to fling the wings apart, very large forces are required at Re relevant to flight in the smallest insects (Miller and Peskin, 2009). The reason for this is as follows: during the fling, the wings are moving rapidly at a high angle of attack, and this leads to the generation of high pressure on the windward side of the wings. Also, the fling leads to the generation of large leading-edge vortices around each wing that are positioned in the vicinity of the leeward side of the wings, and this results in a low-pressure region on the leeward side of the wings. The large pressure difference between the windward and leeward sides of the wings results in a large pressure force acting on the wings which, in turn, leads to a large pressure drag on the wings. Also significant is the large viscous drag acting on the wing due to the low Re. The large pressure and viscous drag together make flinging the wings apart a challenging task. Horridge suggested that the smallest insects might employ drag-based vertical strokes to generate vertical force (Horridge, 1956). Subsequent work emphasized the importance of drag-based strokes in insect flight with Wang's work demonstrating that an idealized dragonfly wing motion supports three-quarters of the insect's weight with drag (Wang, 2004). Similar other studies focused on insect flight have considered high Re and therefore, the low Re regime that is relevant to flight in the smallest insects hasn't been investigated rigorously. A recent study conducted by Jones et al. was focused extensively on the performance of lift and drag-based strokes at low Re with the primary focus being vertical force production (Jones et al., 2015). They had performed their investigations for a rigid and a flexible wing.

A specific flight strategy is a result of compromise among many factors including vertical force generation and therefore, it is important to rigorously investigate other flight factors like stability, aerodynamic efficiency, control, etc. as well (Jones et al., 2015). To further understand flight in the smallest insects, computational fluid dynamics is a convenient tool as it allows for the exploration of a variety of wing kinematics and different combinations of flight parameters which otherwise might be difficult or even impossible to measure directly with experiments.

For our study, we considered four different flexible wings and a rigid wing. We were primarily interested in aerodynamic efficiency and energy considerations. We defined a new dimensional quantity and termed it "pseudo-efficiency". This quantity is equal to the ratio of the average vertical force generated by a wing to the average power delivered by the wing to the surrounding fluid and was used as a measure of energy efficiency. Aerodynamic efficiency was defined as the ratio of the time-averaged vertical force coefficient to the time-averaged net force coefficient. The immersed boundary method was utilized to solve the fully coupled fluid structure interaction problem of a flexible wing immersed in a two-dimensional viscous fluid. For each wing, we conducted a parametric study: Five different stroke plane angles were considered: 0° (horizontal stroke), 22.5° (hybrid stroke), 45° (hybrid stroke), 77.5° (hybrid stroke), 90° (vertical stroke). For each stroke plane angle, we varied the Re and for each Re, we calculated the dimensionless forces as functions of dimensionless time (time was normalized using the stroke period). Further, we calculated the aerodynamic efficiency and the pseudo-efficiency as functions of Re for each stroke plane angle. The main objective of this study was to determine how wing flexibility and stroke plane angle affect aerodynamic efficiency and pseudo-efficiency in the flight of the smallest insects.

Methods

Prescribed Wing Kinematics:

The wing kinematics utilized in this study are identical to those used in similar previous studies (Wang, 2004; Jones et al., 2015). This was a two-dimensional study and therefore, it would be more appropriate to call the kinematics utilized here as the kinematics of the wing chord. The kinematics of the wing chord were defined as follows: -

$$[x(t), y(t)] = \frac{A_0}{2}(1 + \cos(2\pi ft))\,[\cos(\beta), \sin(\beta)] + C_o$$

$$\alpha(t) = \alpha_o + B \sin(2\pi ft)$$

in which [x(t), y(t)] is the position of the center of the wing chord at time t, f is the flapping frequency, β is the stroke plane angle, A_o is the stroke amplitude, a (t) is the angle of attack of the wing, a_o is the mean angle of attack, B is the rotation amplitude, and C_o was used to adjust the initial position of the chord. Fig. 1 illustrates a wing stroke that is governed by thiskinematics. For all parameter combinations, the wing chord length c = 0.1 m, A_o = 0.25 m, f =1 Hz, B = π/4, a_o = π/2, and C_o = 0.2 m for x(t) and 0.3 m for y(t). The stroke plane angles (β) considered were 0°, 22.5°, 45°, 77.5°, and 90°.

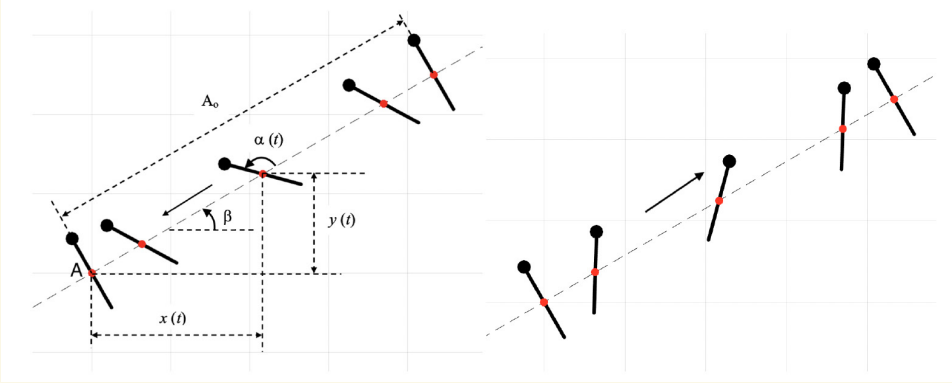

Figure 1. A wing stroke generated by the kinematics described in the methods section. The left part of the figure illustrates the downstroke while the right part illustrates the upstroke. The solid arrows represent the direction of motion of the wing center.

Numerical Method:

We used an open-source two-dimensional computational fluid dynamics code, IB2d, (Battista et al., 2015, 2017, 2018) based on the immersed boundary method developed by Charles Peskin (Peskin, 1972, 1977, 2002) to conduct our investigations. The immersed boundary method has been used to model and study a variety of fluid phenomena such as dynamics of natural and prosthetic heart valves (Griffith et al., 2009), insect flight (Miller and Peskin, 2004, 2005, 2009), jellyfish swimming (Taheri, 2018), and bacterial flagella (Maniyeri et al., 2012). The Navier Stokes equations (in Eulerian form) that govern the fluid behavior are as follows:

$$\rho\left(\frac{\partial u}{\partial t} + (\mathbf{u}(\mathbf{x}, t) \bullet \nabla)\mathbf{u}(\mathbf{x}, t)\right) = -\nabla p(\mathbf{x}, t) + \mu\Delta\mathbf{u}(\mathbf{x}, t) + \mathbf{f}(\mathbf{x}, t), \quad (1)$$

$$\nabla \bullet \mathbf{u}(\mathbf{x}, t) = 0 \quad (2)$$

Here, u(x, t) is the fluid velocity at position x = [x, y] and time t, p(x, t) is the fluid pressure, f(x, t) is the force per unit area applied to the fluid by the immersed boundary. Eq. (2) is the mass conservation equation for incompressible fluid flow. The equations that govern the interaction between the fluid and the immersed boundary are as follows:

$$\mathbf{f}(\mathbf{x}, t) = \int \mathbf{F}(n, t)d(\mathbf{x} - \mathbf{X}(n, t))\, dn, \quad (3)$$

$$\frac{\partial X(n,t)}{\partial t} = \mathbf{U}(\mathbf{X}(n, t)) = \int u(x,\ t)\delta(x\ -\ X(n,\ t))\, d\mathbf{x} \quad (4)$$

Here F(n, t) is the force per unit length applied by the immersed boundary to the fluid as a function of Lagrangian position n and time t. δ (x) is a two-dimensional delta function and X(n, t) gives the Cartesian coordinates at time t of the material point labeled by the Lagrangian parameter n. Eq. (3) applies force from the Lagrangian boundary to the fluid grid, and Eq. (4) evaluates the fluid velocity at the boundary. The boundary is then moved at the local fluid velocity, and this enforces the no-slip boundary condition. Eq. (3) and Eq. (4) couple the Eulerian and Lagrangian variables. In our study, the two-dimensional wing was the immersed boundary.

The forces exerted on the wing by the fluid were non-dimensionalized by $0.5\rho U^2_{rms}c$ where ρ is the fluid density, U_{rms} is the root mean square speed of the center of the wing chord, and c is the chord length. The vertical and horizontal force coefficients are denoted by C_V and C_H , respectively, and the total force coefficient is denoted by C_T. The vertical force generated by the wing is denoted by F_V and the instantaneous power delivered by the wing to the fluid is denoted by P. A horizontal bar above these quantities represents their time-averaged value.

Table 1: Numerical Parameters

Parameter	Value
Grid Resolution	256×256
Length of grid in x direction	6c
Length of grid in y direction	6c
Time step (dt)	1.25e-5t
Spatial step size (dx)	2.35e-2c
Final simulation time	4t
Wing chord length	c
Length of Stroke Plane	2.5c
Fluid density	3047.62618 kg/m^2

We used a chord based Re for our simulations. The Re was defined as follows:

$$Re = \frac{\rho U_{max} c}{\mu} = \frac{\rho \pi f A_o c}{\mu}$$

Here, U_{max} is the maximum speed of the center of the wing chord during one wing stroke, and c is the chord length. The Reynolds numbers considered in our study are 1, 4, 16, 32, 64, and 128. The fluid viscosity was varied to alter the Re. The density (ρ) was kept constant at 3047.63 kg/m^2 . We used an open-source software called VisIt, developed, and maintained by Lawrence Livermore National Laboratory for flow visualization and used the data analysis software within IB2d for performing data analysis on the simulation data (Childs, 2012; Battista et al., 2017). Table 1 summarizes the numerical parameters that were used for the simulations in our study (c is the chord length and t is the stroke period).

Grid Convergence Study:

Table 2: Average percent difference in force coefficients over the last two wing beats between different grid resolutions at $Re = 128$ and $\beta = 0°, 45°, 90°$ for the rigid wing

β	Grids	Average % Difference (C_V)	Average % Difference (C_H)
0°	128×128 vs. 256×256	22.39	0.2274
	256×256 vs. 512×512	4.3687	3.1439
45°	128×128 vs. 256×256	26.8348	37.6068
	256×256 vs. 512×512	3.4384	0.2983
90°	128×128 vs. 256×256	1.8934	0.7861
	256×256 vs. 512×512	0.4544	2.0455

To test for spatial convergence, we compared three different grid resolutions: a uniform 128 × 128 discretization, a uniform 256 × 256 discretization, and a uniform 512 × 512 discretization. We considered the following three stroke plane angles for our grid convergence study: 0°, 45°, and 90°. We performed our simulations for the rigid wing at Re =128. This choice was motivated by the difficulty of resolving thin boundary layers and vortex separation for the rigid wing at Re = 128. The force coefficients for the three grid resolutions showed overall good agreement for $\beta = 0°$ and $\beta = 90°$ (Fig. 2). The three grid resolutions were compared by calculating the average percent difference in force coefficients between the selected grid and the next finest grid over the last two wing beats (Table 2). The 256 × 256 grid was used for all simulations in our study because the average percent difference in force coefficients between this grid and the next finest grid (512 x 512) was < 5 % for all the three stroke plane angles. The grid convergence study was performed using a custom MATLAB code.

Wing Geometry:
Rigid Wing:

To model the rigid wing, we used 75 Lagrangian points. The only fiber model used for the rigid wing simulations was target points. They were used to prescribe the motion of all the Lagrangian points. Each Lagrangian point was associated with a target point and was connected to its target point using a stiff spring, i.e., a spring with zero resting length. The deformation energy of the stiff spring is as follows:

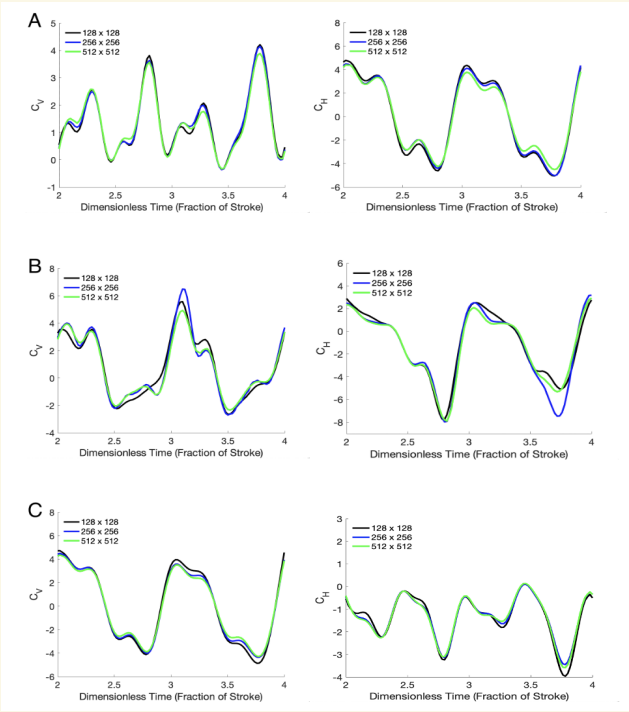

Figure 2. C_V and C_H as functions of dimensionless time for the rigid wing at Re = 128 and (A) $\beta = 0°$, (B) $\beta = 45°$, and (C) $\beta = 90°$. The coefficients were calculated for the following three grid resolutions: 128 x 128, 256 x 256, and 512 x 512.

$$E_T(\mathbf{X}_M) = \frac{1}{2} k_T \| X_M - X_M^T \|^2,$$

where k_T is the stiffness value of the stiff spring and X_M and X^T_M are the coordinates of the Lagrangian point and the target point, respectively. The corresponding deformation forces are as follows:

$$\mathbf{F}_T = - \frac{\partial E_T}{\partial X_M} = < - k_T(x_M - x_M^T), - k_T(y_M - y_M^T) >$$

It is standard for the stiffness k_T to be very large to move the Lagrangian points in a prescribed manner. The non-dimensional stiffness value k_T' for the rigid wing was 9.6×10^4. k_T was non- dimensionalized in the following manner:

$$k_T' = \frac{k_T}{\rho U_{rms}^2 c}$$

Flexible Wing:

We modeled four different flexible wings for our study. Three different fiber models were used for all the flexible wings - target points, non-invariant beams, and springs. 75 Lagrangian points were used to model each wing and only the first 25 points starting from the leading edge were tethered to target points. The remainder of the wing was allowed to bend as it interacted with the fluid. The non-dimensional stiffness value of the spring associated with the target points was equal to 9.6×10^4 for all the flexible wings. This value was chosen arbitrarily, and it was large enough to ensure that the rigid portion of the flexible wings was moving as per the prescribed kinematics.

Two new fiber models that were used here are springs and non-invariant beams. Springs were used to model the resistance to stretching between successive Lagrangian points. We used Hookean springs to model the connections between successive Lagrangian points. Hookean springs were used because they are relatively easier to implement than other non-linear springs for the purpose of preventing the stretching of the wing during its motion. The Hookean springs implemented in this study prevented the stretching of the wing during its motion to a satisfactory extent. The elastic potential energy of a Hookean spring is as follows:

$$E_{spring} = \frac{1}{2} k_S (|| X_{SL} - X_M|| - R_L)^2,$$

where k_s is the spring stiffness, R_L is the resting length of the spring, and X_M and X_{SL} are the master and slave node coordinates, respectively.

The corresponding deformation force is given by a derivative of the elastic potential energy:

$$F_{spring} = k_S(1 - \frac{R_L}{|| X_{SL} - X_M||}) < x_{SL} - x_M, y_{SL} - y_M >$$

The non-dimensional spring stiffness k_s' was equal to 9.6×10^8 for all the flexible wings and the resting length R_L was equal to 0.0135 m which was the distance between successive Lagrangian points. This large non-dimensional value of spring stiffness was chosen to ensure minimal stretching of the wings during the simulations. k_s was non-dimensionalized in the following manner:

$$k_S' = \frac{k_S}{\rho U_{rms}^2 c}$$

Non-invariant beams were used to model the resistance to bending between 3 successive Lagrangian points. For a set of 3 successive Lagrangian points, say X_L, X_M, and X_R, a non-invariant beam was used to connect the three points. This model assumes a prescribed curvature in both x and y components between the 3 Lagrangian points with corresponding bending stiffness k_{NIB} (Battista et al., 2017). The bending deformation forces are as follows:

$$F_{beam} = k_{NIB} \frac{\partial^4}{\partial n^4} (\mathbf{X}(n, t) - \mathbf{X}_b(n, t))$$

where X(n, t) is the current Lagrangian configuration at time t, $X_b(n, t)$ is the preferred configuration of the non-invariant beam at time t, and k_{NIB} is the bending stiffness of the non-invariant beam. Non-invariant beams were used to connect successive triplets of Lagrangian points over the entire wing for all the flexible wings. The non-dimensional bending stiffness of all non-invariant beams was the same for a specific flexible wing. As mentioned earlier, we modeled four different flexible wings. The non-dimensional bending stiffness values (k_{NIB}') for the four wings are as follows: 3.2×10^{10} (most flexible), 3.4×10^{10}, 6.8×10^{10}, 9.6×10^{10} (least flexible). Wing flexibility is directly related to the non-dimensional bending stiffness value. Wing flexibility increases as k_{NIB}' decreases and it decreases as k_{NIB}' increases. The prescribed curvature in both x and y directions was set to 0 for all the flexible wings. k_{NIB} was non-dimensionlized in the following manner:

$$k'_{NIB} = \frac{k_{NIB}}{\rho U_{rms}^2 c^3}$$

The following are the equations that were used to calculate the aerodynamic performance parameters for our study:

$$C_V = \frac{F_V}{\rho U_{rms}^2 c}$$

$$C_H = \frac{F_H}{\rho U_{rms}^2 c}$$

$$C_T = \frac{F_T}{\rho U_{rms}^2 c}$$

$$C_T = \frac{F_T}{\rho U_{rms}^2 c}$$

$$F_T = \sqrt{F_H^2 + F_V^2}$$

$$\text{Aerodynamic Efficiency} = \frac{\overline{C_V}}{\overline{C_T}}$$

$$\text{Pseudo-efficiency} = \frac{\overline{F_V}}{P}$$

Results

Rigid Wing:

We performed simulations for the rigid wing using the prescribed kinematics presented in the methods section. Each simulation consisted of four stroke cycles. Calculation of aerodynamic forces, aerodynamic efficiency, and pseudo-efficiency was done using simulation data for only the third and fourth stroke cycles that exhibited periodic variation of aerodynamic forces with non-dimensional time. Time was normalized using the stroke period. C_V and C_H are shown as functions of dimensionless time during the third and fourth stroke cycles for all Re considered in this study for $\beta = 0°$ (Fig. 3), the hybrid strokes (Fig. 4), and $\beta = 90°$ (Fig. 5). For the horizontal stroke ($\beta = 0°$), for both the half-strokes, the magnitude of the instantaneous horizontal force coefficient decreased as the Re increased. The magnitude of the instantaneous vertical force coefficient decreased with increasing Re until Re = 64, and then increased with increasing Re. This was true for wing rotation at the beginning of half-strokes up until mid- translation. For the majority of the remaining stroke, the magnitude of instantaneous C_V decreased with increasing Re until Re = 16, and then increased with increasing Re. For the horizontal stroke, at higher Re, C_V was positive for almost the entire stroke while at lower Re, C_V was positive during wing rotation at the beginning of half-strokes and during majority of the translation phase and was negative during wing rotation at the end of half-strokes.

For $\beta = 22.5°$, for the downstroke, the magnitude of instantaneous C_H decreased with increasing Re. For the upstroke, the magnitude of instantaneous C_H decreased with increasing Re for wing rotation at the beginning up until mid-translation. For most of the upstroke beyond mid-translation, the magnitude of instantaneous C_H decreased with increasing Re until Re = 64, and then increased with increasing Re. The magnitude of instantaneous C_V decreased with increasing Re for the downstroke. For the upstroke, the magnitude of instantaneous C_V decreased with increasing Re for wing rotation at the beginning up until mid-translation. For most of the remaining upstroke, the magnitude of instantaneous C_V decreased with increasing Re until Re = 32, and then increased with increasing Re. At both low and high Re, C_V was positive for most of the downstroke. For the upstroke, at both low and high Re, C_V was mostly negative.

For β = 45°, the magnitude of both the instantaneous horizontal force coefficient and the instantaneous vertical force coefficient decreased as the Re increased. C_V was positive during the downstroke and negative during the upstroke. For β = 77.5°, for the downstroke, the magnitude of instantaneous C_H decreased with increasing Re until Re = 16, and then increased

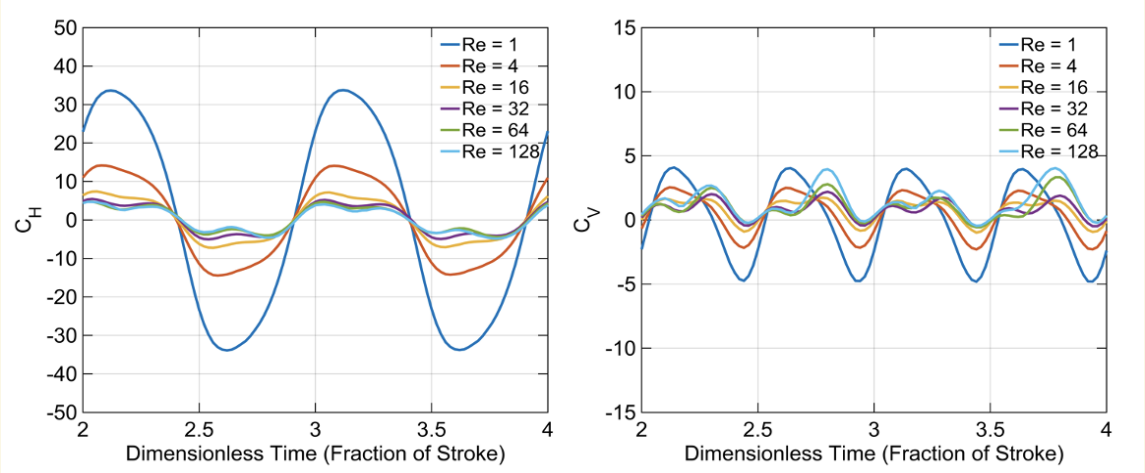

Figure 3. C_H and C_V as functions of dimensionless time during the third and fourth stroke cycles for the horizontal stroke. (Rigid Wing)

with increasing Re. For the upstroke, the magnitude of instantaneous C_H decreased with increasing Re. This was valid from the beginning of the upstroke up until mid-translation. For most of the remainder of the translation phase, the magnitude of C_H increased with increasing Re, and it decreased with increasing Re for wing rotation at the end of the upstroke. As far as C_v is concerned, the magnitude of instantaneous C_v decreased with increasing Re for both the upstroke and the downstroke. C_v was primarily positive for the downstroke and negative for the upstroke.

For the vertical stroke (β = 90°), the variation in the magnitude of instantaneous C_H with increasing Re was almost identical to the variation of the magnitude of instantaneous C_v with increasing Re for the horizontal stroke. The magnitude of instantaneous C_v decreased with increasing Re for the vertical stroke. Like β = 45°, C_v was positive during the downstroke and negative during the upstrokes.

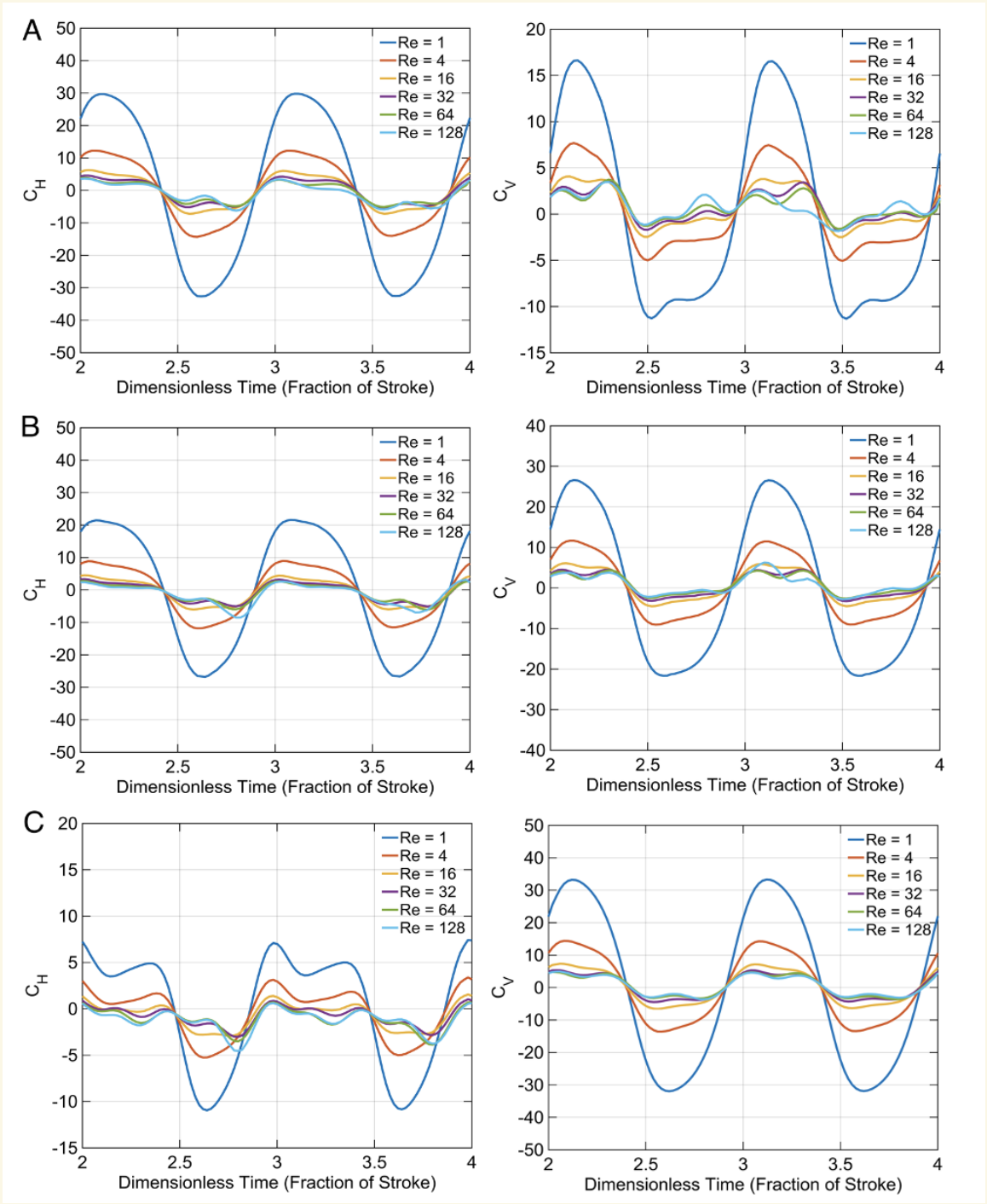

Figure 4. C_H and C_V as functions of dimensionless time during the third and fourth stroke cycles for (A) $\beta = 22.5°$, (B) $\beta = 45°$, and (C) $\beta = 77.5°$. (Rigid Wing)

As far as maximum Cv value is concerned, for the horizontal stroke, at higher Re, Cv achieved its maximum value during wing rotation at the end of the upstroke while at lower Re, Cv achieved its maximum value during wing rotation at the beginning of the downstroke.

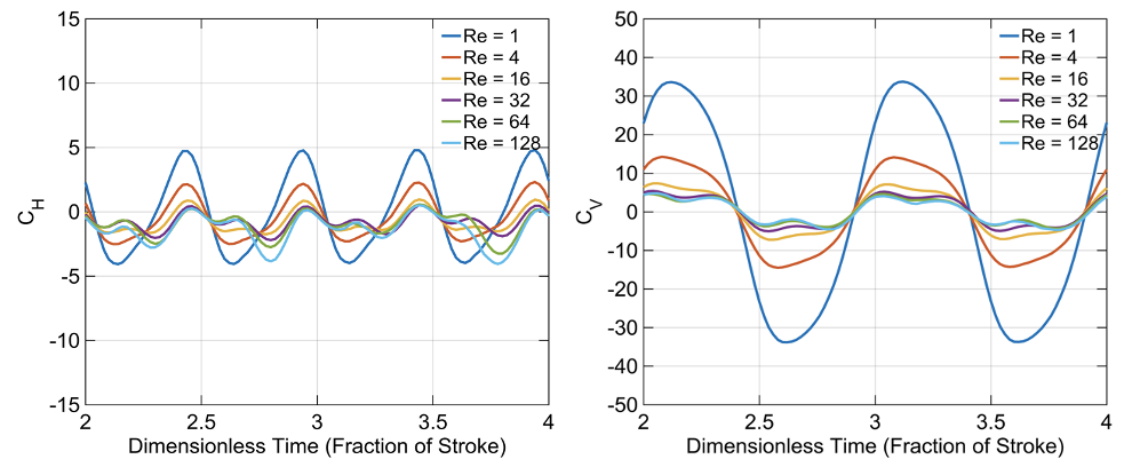

Figure 5. C_H and C_V as functions of dimensionless time during the third and fourth stroke cycles for the vertical stroke. (Rigid Wing)

For β = 22.5°, at lower Re, Cv achieved its maximum value during wing rotation at the beginning of the downstroke while for higher Re, Cv achieved its maximum value during wing rotation at the end of the downstroke. For β = 45°, β = 77.5°, and β = 90°, Cv achieved its maximum value during wing rotation at the beginning of the downstroke for both higher and lower Re. For β = 0° and β = 22.5°, maximum CH values were higher than maximum Cv values while for β = 45°, β = 77.5°, and β = 90°, maximum Cv values were higher than maximum CH values. Maximum Cv value decreased as Re increased for β = 22.5°, β = 45°, and β = 90°. For the horizontal stroke, maximum Cv value decreased as Re increased until Re = 16, and then increased as Re increased. For β = 77.5°, maximum Cv value decreased as Re increased until Re = 64, and then increased as Re increased. The basis for some of these results can be understood by looking at the vorticity plots of the fluid around the wing chord at Re = 4 and Re = 128 during the fourth stroke cycle (Fig. 6). Since the wing kinematics were the same for all the five stroke plane angles, the vorticity plots were quantitatively the same for all stroke plane angles at a specific Re. Vorticity plot for β = 22.5°, β = 45°, β = 77.5°, and β = 90°, are equivalent to the vorticity plots for the horizontal stroke rotated in the counterclockwise sense by 22.5°, 45°, 77.5°, and 90°, respectively. Therefore, vorticity plots for only the horizontal stroke are included in this paper.

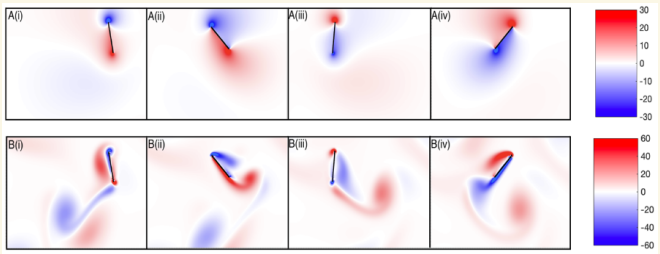

Figure 6. Vorticity plots of the fluid during the fourth stroke cycle at (A) *Re* = 4 and (B) *Re* = 128 shown at (i) the beginning of downstroke, (ii) midway through downstroke, (iii) beginning of downstroke, (iv) midway through upstroke. The color map displays the fluid vorticity (Red - counterclockwise rotation, Blue - clockwise rotation) (Rigid Wing).

Fig. 6 shows the vorticity plots of the fluid around the rigid wing during the fourth stroke cycle at Re = 4 and Re = 128. For Re = 4, leading edge (LEV) and trailing edge (TEV) vortices were formed during wing rotation at the beginning of the downstroke, and they remained attached to the wing during the entire translation phase of the downstroke. These vortices were shed during wing rotation at the end of the downstroke and new vortices were formed during wing rotation at the beginning of the upstroke. They remained attached to the wing during the entire translation phase of the upstroke and were shed during wing rotation at the end of the upstroke. For Re = 128, the vorticity plots were significantly different. A LEV and a TEV were formed during wing rotation at the beginning of the downstroke. The LEV remained attached to the wing during the entire translation phase of the downstroke while the TEV was shed midway through the downstroke. The LEV was shed during wing rotation at the end of the downstroke. New vortices were formed during wing rotation at the beginning of the upstroke. Like the downstroke, the LEV remained attached to the wing during the entire translation phase of the upstroke while the TEV was shed midway through the upstroke. As can be concluded, vortex shedding for Re = 4 was symmetric while that for Re = 128 was asymmetric.

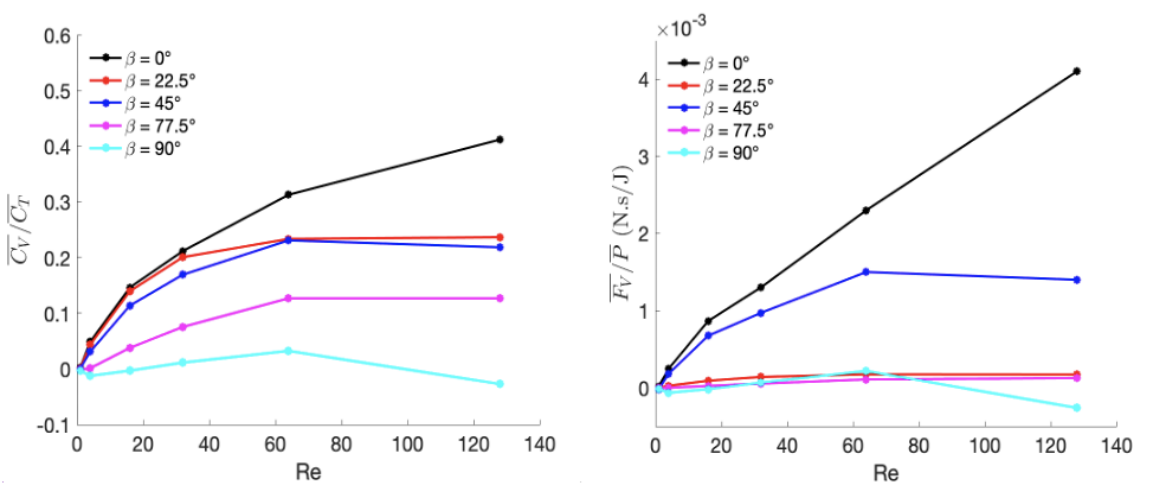

Figure 7. $\overline{C_V}/\overline{C_T}$ as a function of *Re* for all stroke plane angles considered in this study (to the left of the figure) and $\overline{F_V}/\overline{P}$ as a function of *Re* for all stroke plane angles considered in this study (to the right of the figure) (Rigid Wing).

Aerodynamic efficiency (C_v/C_T) and pseudo-efficiency (F_v/P) were calculated as functions of Re for the rigid for all stroke plane angles considered in this study. C_v and C_T were averaged over the third and fourth stroke cycles and similarly, pseudo-efficiency was calculated using the simulation data for only the third and fourth stroke cycles.

Fig. 7 shows the variation of these quantities with Re for the rigid wing for all stroke plane angles considered in this study. For both $\beta = 0°$ and $\beta = 77.5°$, C_v/C_T and F_v/P increased monotonically with increasing Re. For $\beta = 22.5°$, aerodynamic efficiency increased monotonically with increasing Re while pseudo-efficiency increased with increasing Re until Re = 64 and then decreased with increasing Re. For $\beta = 45°$ and $\beta = 90°$, both C_v/C_T and F_v/P increased with increasing Re until Re = 64 and then decreased with increasing Re. The horizontal stroke generated more C_v/C_T than the hybrid and the vertical strokes at all Re considered in this study. Same was the case for the pseudo-efficiency (F_v/P).

Flexible Wings:

As mentioned earlier, we modeled four different flexible wings for our study. The focus of this section is on the variation of aerodynamic efficiency and pseudo-efficiency with wing flexibility at Re > 100 and Re relevant to small insect flight for all stroke plane angles considered in this study:

Variation of Aerodynamic Efficiency with wing flexibility:

Fig. 8 shows aerodynamic efficiency (C_v/C_T) as a function of Re for all the wings at all stroke plane angles considered in this study. At Re > 100, for $\beta = 0°$ and $\beta = 45°$, C_v/C_T increased with increasing wing flexibility until $k_{NIB}' = 6.8 \times 10^{10}$, and then decreased with increasing wing flexibility. For $\beta = 22.5°$, C_v/C_T increased with increasing wing flexibility until $k_{NIB}' = 3.4 \times 10^{10}$, and then showed a decrease for the most flexible wing. For $\beta = 77.5°$ and $\beta = 90°$, C_v/C_T initially decreased with increasing flexibility, then increased with increasing wing flexibility until $k_{NIB}' = 3.4 \times 10^{10}$, and then showed a decrease for the most flexible wing.

At Re pertinent to small insect flight, for $\beta = 0°$ and $\beta = 45°$, C_v/C_T initially decreased with increasing wing flexibility, then increased with increasing wing flexibility until $k_{NIB}' = 6.8 \times 10^{10}$, and then decreased with increasing flexibility. For $\beta = 22.5°$ and $\beta = 77.5°$, C_v/C_T decreased monotonically with increasing wing flexibility. For $\beta = 90°$, C_v/C_T decreased with increasing wing flexibility until $k_{NIB}' = 3.4 \times 10^{10}$, and then showed an increase for the most flexible wing.

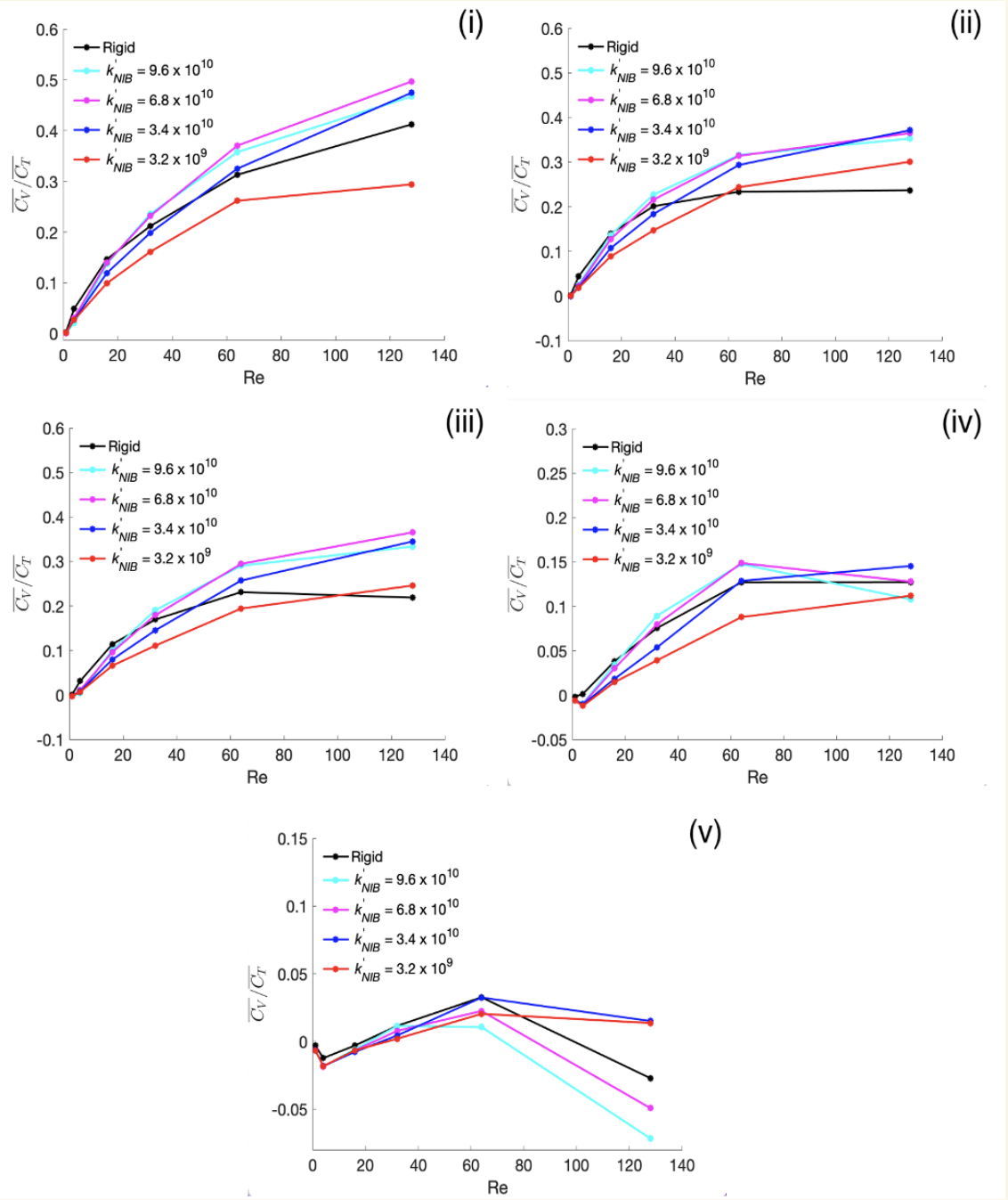

Figure 8. $\overline{C_V}/\overline{C_T}$ as a function of Re for all wings considered in this study for $(i): \beta = 0°, (ii): \beta = 22.5°, (iii): \beta = 45°, (iv): \beta = 77.5°, (v): \beta = 90°$.

Variation of Pseudo-efficiency with wing flexibility:

Fig. 9 shows pseudo-efficiency (F_v/P) as a function of Re for all the wings at all stroke plane angles considered in this study. At Re > 100, for $\beta = 0°$ and $\beta = 45°$, F_v/P initially decreased rapidly with increasing flexibility, and then decreased monotonically with increasing flexibility at a relatively smaller rate.

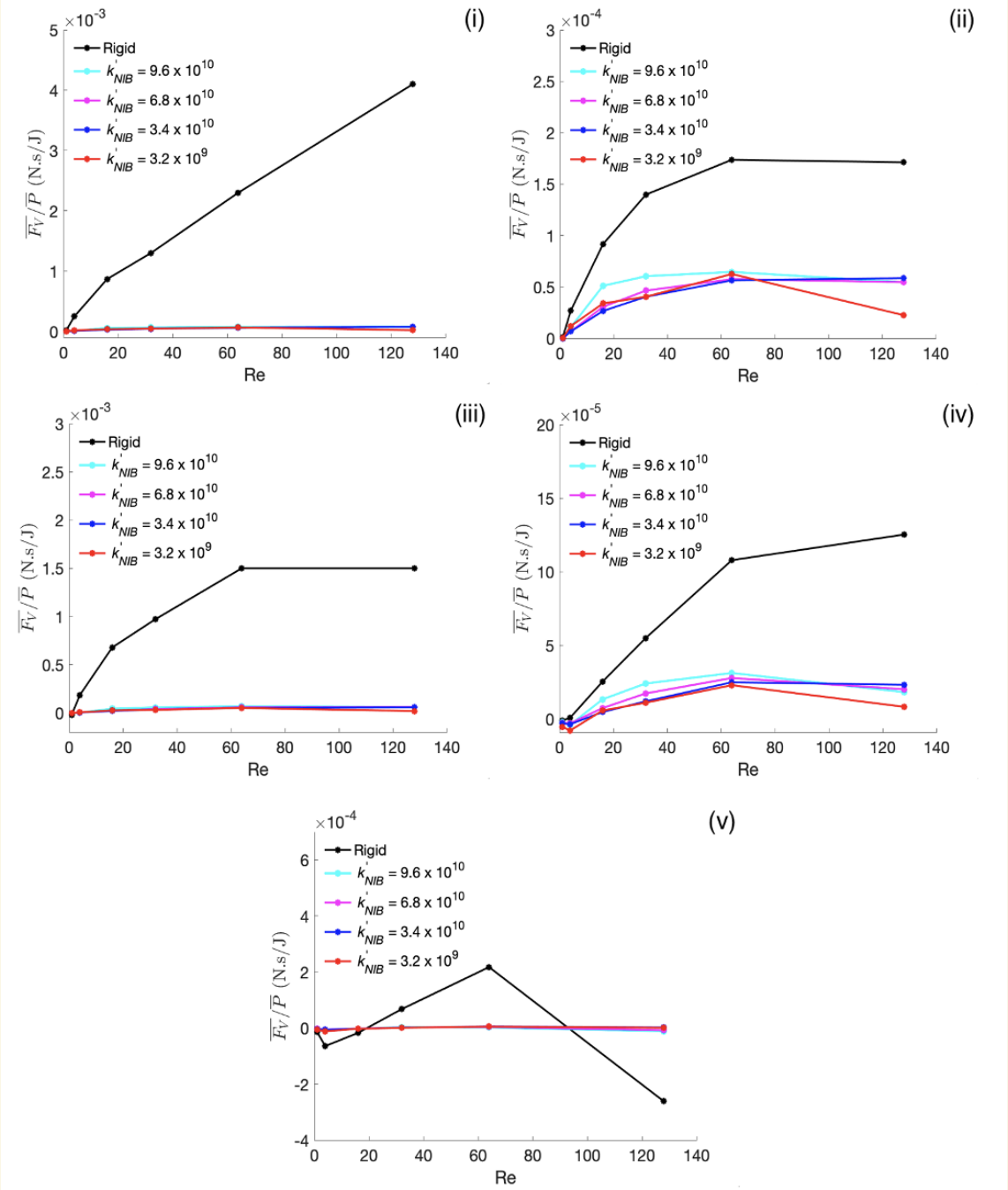

Figure 9. $\overline{F_V}/\overline{P}$ as a function of *Re* for all wings considered in this study for $(i) : \beta = 0°, (ii) : \beta = 22.5°, (iii) : \beta = 45°, (iv) : \beta = 77.5°, (v) : \beta = 90°$.

For β = 22.5°, F_V/P decreased with increasing wing flexibility until $k_{NIB}' = 6.8 \times 10^{10}$, then showed an increase for $k_{NIB}' = 3.4 \times 10^{10}$, and then decreased with further increase in flexibility. For β = 77.5°, F_V/P initially decreased with increasing wing flexibility, then increased with increasing flexibility until $k_{NIB}' = 3.4 \times 10^{10}$, and then showed a decrease for the most flexible wing. For β = 90°, F_V/P increased with increasing wing flexibility until $k_{NIB}' = 3.4 \times 10^{10}$, and then showed a slight decrease for the most flexible wing.

At Re relevant to the flight of the smallest insects, for $\beta = 0°$, $\beta = 22.5°$, and $\beta = 45°$, F_v/P decreased with increasing wing flexibility until $k_{NIB}' = 3.4 \times 10^{10}$, and then increased with increasing wing flexibility. For $\beta = 77.5°$, F_v/P decreased monotonically with increasing wing flexibility. For $\beta = 90°$, F_v/P increased with increasing wing flexibility until $k_{NIB}' = 6.8 \times 10^{10}$ and then decreased with increasing flexibility.

Discussion

The results of this study imply that: (1) at Re relevant to small insect flight, aerodynamic efficiency decreases monotonically with increasing stroke plane angle regardless of wing flexibility; (2) at Re pertinent to the flight of the smallest insects, adding flexibility to a rigid wing depreciates aerodynamic efficiency regardless of the stroke plane angle - a rigid wing is aerodynamically more efficient than flexible wings at all stroke plane angles. Implication (1) agrees with the paper of Jones et al. where they suggested that for the smallest flying insects, a lift-based mechanism generates more C_v/C_T than a drag-based mechanism (vertical stroke) (Jones et al., 2015).

Our study also took energy considerations into account. As stated in the introduction section, we defined a new dimensional quantity, pseudo-efficiency, which is the ratio of the average vertical force generated by a wing to the average power delivered by the wing to the surrounding fluid, to establish a measure of energy efficiency. The results of our study imply that: (1) at Re relevant to the flight of the smallest insects, pseudo-efficiency decreases monotonically with increasing stroke plane angle regardless of wing flexibility, (2) at Re relevant to small insect flight, adding flexibility to a rigid wing deteriorates pseudo-efficiency regardless of the stroke plane angle - a rigid wing is energetically more efficient than flexible wings at all stroke plane angles.

Flexibility has been shown to play an important role in drag reduction in biological structures (Miller and Peskin, 2004, 2009; Alben et al., 2002). Our results indicate that it plays an important role in augmenting aerodynamic efficiency in insect flight at high Re. However, our study has also shown that it negatively impacts energy efficiency in insect flight. In general, a rigid wing outperforms flexible wings in terms of energy efficiency in insect flight.

Conclusions

Our study indicates that increasing the stroke plane angle negatively impacts aerodynamic efficiency and pseudo-efficiency for all wing flexibilities and adding flexibility to a rigid wing deteriorates both its aerodynamic efficiency and pseudo-efficiency at all strokes a rigid wing deteriorates both its aerodynamic efficiency and pseudo-efficiency at all stroke plane angles in the flight of the smallest insects. A drag-based vertical stroke is inferior to both horizontal and hybrid strokes in terms of pseudo-efficiency and aerodynamic efficiency at almost all Re regardless of the wing flexibility, and this could explain why we are not aware of any small insects that use drag-based strokes at very low Re. A frequently observed trend in our results was that both aerodynamic efficiency and pseudo-efficiency increased with increasing Re. The smallest insects, however, restrict their flight to low Re. This was a simplified study that utilized 2D kinematics and symmetrical strokes. Further insight could be obtained into the flight of the smallest insects by considering additional flight strategies like bristled wings and wing-wing interactions.

Our study only analyzed aerodynamic efficiency and pseudo-efficiency as the driving factors behind the choice of flight mechanism in the smallest insects. However, there are several other factors that influence the choice of flight strategy in the smallest insects. Stability and control, maneuverability, and wing strength are some of the many factors that influence the type of flight mechanisms that the smallest insects employ. It is important to consider these factors while investigating the flight of the smallest insects in the future to gain a more complete understanding of small insect flight. The overall flight strategy is a result of compromise among many factors and not just aerodynamic efficiency and energy efficiency. Further, the wing strokes need not always be symmetrical like they were in this study. Many insects have been observed to use asymmetrical strokes (Jones et al., 2015), i.e., strokes where the upstroke and the downstroke are asymmetrical. The tiny insect Encarsia formosa, for instance, has been observed to have a faster upstroke than downstroke (Weis-Fogh, 1973). Future two-dimensional studies should implement asymmetrical strokes to arrive at more practical results. The asymmetry of strokes coupled with the vortical asymmetry presented in fig. 6 could provide more insight.

This study was primarily two-dimensional in nature, and it would certainly differ from a three-dimensional study that more closely mimics real life insect flight. A two-dimensional study fails to capture the spanwise flow effects observed in three dimensions.

These effects may lead to vortex shedding patterns and crossflow that are different from those observed in two-dimensions which, in turn, could result in the aerodynamic performance of 3-D wings being different from that of 2-D wings. Also, since our study was two-dimensional in nature, the wing flexibility was constant along the span. In future three-dimensional studies, the degree of flexibility along the wingspan could be varied to simulate real life insect wings more closely and thus, arrive at more accurate results. These studies could also consider wing-wing interactions like the clap and fling mechanism that is believed to be employed by the smallest insects (Weis-Fogh, 1973). They could also consider the impact of the presence of the insect body between the two wings on the overall flow behavior. We utilized a linear stroke plane in our study. However, the wing tips of many insects have been found to trace out patterns shaped like ovals, parabolas, or a simple figure of eight. Future work could employ these patterns to investigate flight in the smallest insects more rigorously. Extensive efforts are required in the future to completely unravel the complexities of flight in the smallest insects.

References

Wang, Z.J. Dissecting Insect Flight. Annu. Rev. Fluid Mech. 2005, 37, 183-210.

Naranjo, S.E. Assessing insect flight behavior in the laboratory: a primer on flight mill methodology and what can be learned. Annals of the Entomological Society of America 2019, 112, 182-199.

Bodino, N.; Cavalieri, V.; Dongiovanni, C.; Simonetto, A.; Saladini, M.A.; Plazio, E.; Gilioli, G.; Molinatto, G.; Saponari, M.; Bosco, D. Diseprsal of Philaneus spumarius (Hemiptera: Aphrophoridae), a vector of Xylella fastidiosa, in olive grove and meadow agroecosys tems. Environmental entomology 2021, 50, 267-279.

Cameron, P.; Wigley, P.; Charuchinda, B.; Walker, G.; Wallace, A. Farm-scale dispersal of Bacte ricera cockerelli in potato crops measured using Bt mark-capture techniques. Entomolo gia Experimentalis et Applicata 2013, 148, 161-171.

Jones, S.; Laurenza, R.; Hedrick, T.L.; Griffith, B.E.; Miller, L.A. Lift vs. drag based mechanisms for vertical force production in the smallest flying insects. Journal of Theoretical Biology 2015, 384, 105-120.

WANG, Z.z.; LIU, Y.q.; Min, S.; HUANG, J.h.; CHEN, X.x. Parasitoid wasps as effective biologi -cal control agents. Journal of Integrative Agriculture 2019, 18, 705-715.

Cook, D.; Herbert, A.; Akin, D.S.; Reed, J. Biology, crop injury, and management of thrips (Thysanoptera: Thripidae) infesting cotton seedlings in the United States. Journal of Integrated Pest Management 2011, 2, B1-B9.

Ellington, C.P. The novel aerodynamics of insect flight: applications to micro-air vehicles. Jour nal of Experimental Biology 1999, 202, 3439-3448.

Liu, H.; Ravi, S.; Kolomesnkiy, D.; Tanaka, H. Biomechanics and biomimetics in insect inspired flight systems. Philosophical Transactions of the Royal Society B: Biological Sciences 2016, 371, 201503090.

Wang, Z.J.; The role of drag in insect hovering. Journal of Experimental Biology 2004, 207, 4147-4155.

Jensen, M. Biology and physics of locust flight. III. The aerodynamics of locust flight. Philosophical Transactions of the Royal Society of London. Series B, Biological Sciences 1956, 239, 511-552.

Cloupeau, M.; Devillers, J.; Devezeaux, D. Direct measurements of instantaneous lift in desert locust, comparison with Jensen's experiments on detached wings. Journal of Experimental Biology 1979, 80, 1-15.

Wilkin, P.J.; Williams, M.H. Comparison of the aerodynamic forces on a flying sphingid moth with those predicted by quasi-steady theory. Physiological zoology 1993, 66, 1015-1044.

Hollick, F. The flight of the dipterous fly Muscina stabulans Fallen. Philosophical Transac tions of the Royal Society of London. Series B, Biological Sciences 1940, 230, 357-390.

Nachtigall, W. Insects in Flight:A Glimpse Behind the Scenes in Biophysical Research; Mc Graw Hill: New York, 1973.

Demoll, R.; others. Der Flug der Insekten und der Vögel. Naturwissenschaften 1919, 7, 480-482.

Weis-Fogh, T.; Jensen, M. Biology and physics of locust flight. I. Basic principles in insect flight. A critical review. Philosophical Transactions of the Royal Society of London. Series B, Biological Sciences 1956, 239, 415-458.

Von Holst, E.; Kuchemann, D. Biological and aerodynamical problems of animal flight. The Aeronautical Journal 1942, 46, 39-56.

Dudley, R.; Ellington, C. Mechanics of forward flight in bumblebees: II. Quasi-steady lift and power requirements. Journal of Experimental Biology 1990, 148, 53-88.

Vogel, S. Flight in drosophila: III. Aerodynamic characteristics of fly wing sand wing mod els. Journal of Experimental Biology 1967, 46, 431-443.

Nabawy, M.R.; Crowther, W.J. The role of the leading edge vortex in lift augmentation of steadily revolving wings: a change in perspective. Journal of the Royal Society Inter face 2017, 14, 20170159.

Eldredge, J.D.; Jones, A.R. Leading-edge vortices: mechanics and modeling. Annual Re view of Fluid Mechanics 2019.

Ellington, C.P.; van den Berg, C.; Willmott, A.P.; Thomas, A.L.R. Leading-edge vortices in insect flight. Nature 1996, 384, 626-630.

Dickinson, M.; Lehmann, F.; Sane, S. Wing Rotation and the Aerodynamic Basis of Insect Flight. Science 1999, 284, 1954-1960.

Williams, E.; Murphy, D. Wing Flapping by a Tiny Parasitoid Wasp. Bulletin of the American Physical Society 2020.

Sarig, A.; Ribak, G. To what extent can the tiny parasitoid wasps, Erectmocerus mundus, fly upwing? Journal of Applied Entomology 2021.

Burrows, M.; Dorosenko, M. Take-off mechanisms in parasitoid wasps. Journal of Experimental Biology 2017, 220, 3812-3825.

Miller, L.A.; Peskin, C.S. When vortices stick: an aerodynamic transition in tiny insect flight. J Exp Biol 2004, 207, 3073-88.

Miller, L.A., Peskin, C.S. A computational fluid dynamics study of 'clap and fling' in the smallest insects. J Expl Biol 2005, 208, 195-212.

Miller, L.A., Peskin, C.S. Flexible clap and fling in tiny insect flight. J Expl Biol 2009, 212, 3076-90.

Wang, Z.J. Two dimensional mechanism for insect hovering. Physical review letters 2000, 85, 2216.

Weis-Fogh, T. Quick estimates of flight fitness in hovering animals, including novel mechanisms for lift production. J Expl Biol 1973, 59, 169-230.

Sane, S.P. The aerodynamics of insect flight. J Expl Biol 2003, 206, 4191-208.

Weis-Fogh, T. Unusual mechanisms for the generation of lift in flying animals. Scientific Ameri can 1975, 233, 80-87.

Ellington, C.P. The aerodynamics of hovering insect flight, III. Kinematics. Philos. Trans. R. Soc. Lond. B Biol. Sci. 1984, 305, 41-78.

Horridge, G.A.; others. The flight of very small insects 1956.

Battista, N.A.; Baird, A.J.; Miller, L.A. A mathematical model and MATLAB code for mus cle-fluid-structure simulations. Integrative and comparative biology 2015, 55, 901-911.

Battista, N.A.; Strickland, W.C.; Barrett, A.; Miller, L.A. IB2d Reloaded: a more powerful Py thon and MATLAB implementation of the immersed boundary method. Math. Method. Appl. Sci 2017 https://doi.org/10.1002/mma.4708 , 1-26.

Battista, N.A.; Strickland, W.C.; Barrett, A.; Miller, L.A. IB2d Reloaded: A more powerful Python and MATLAB implementation of the immersed boundary method. Mathemati cal Methods in the Applied Sciences 2018, 41, 8455-8480.

Peskin, C.S. Flow patterns around heart valves: a numerical method. Journal of computational physics 1972, 10, 252-271.

Peskin, C.S. Numerical analysis of blood flow in the heart. Journal of computational physics 1977, 25, 220-252.

Peskin, C.S. The immersed boundary method. Acta Numerica 2002, 11, 479-517.

Griffith, B.E.; Luo, X.; McQueen, D.M.; Peskin, C.S. Simulating the fluid dynamics of natural and prosthetic heart values using the immersed boundary method. Interna tional Journal of Applied Mechanics 2009, 1, 137-177.

Taheri, A. Lagrangian coherent structure analysis of jellyfish swimming using immersed bound ary fsi simulations. J. of Mech. and Civil Engineering 2018, 15, 69-74.

Maniyeri, R.; Suh, Y.K.; Kang, S.; Kim, M.J.; Numerical study on the propulsion of a bacterial flagellum in a viscous fluid using an immersed boundary method. Computers & fluids 2012, 62, 13-24.

Childs, H. VisIt: An end-user tool for visualizing and analyzing very large data 2012.

Alben, S.; Shelley, M.; Zhang, J. Drag reduction through self-similar bending of a flexible body. Na ture 2002, 420, 479-481.

Lighthill, M.J.; On the Weis-Fogh mechanism of lift generation. Journal of Fluid Mechanics 1973, 60, 1-17.